JOURNAL OF THERMOPHYSICS AND HEAT TRANSFER
Vol. 7, No. 2, April–June 1993

Density Measurements in an Expanding Flow Using Holographic Interferometry

Surendra P. Sharma* and Stephen M. Ruffin†
NASA Ames Research Center, Moffett Field, California 94035
Scott A. Meyer‡ and Walter D. Gillespie‡
Stanford University, Stanford, California 94305
and
Leslie A. Yates†
Eloret Institute, Palo Alto, California 94303

A nonequilibrium expansion of nitrogen through a two-dimensional nozzle of a reflected shock tunnel is investigated with laser holography, time-resolved pressure measurements, and emission spectroscopy to characterize the flowfield for future vibrational relaxation measurements. A two-dimensional computation is used to simulate the nozzle flowfield. Synthetic holograms are generated using the computed density profiles and are compared with the experimental holograms. Also, using a quasi-one-dimensional approximation, populations for each vibrational level are computed by 1) solving the master equations, and 2) using the Landau-Teller formulation. Computational accuracy of both models is assessed against the experimental data.

I. Introduction

EXPANDING flows are the least understood hypersonic flow phenomena. In contrast to the relaxation behind a shock wave, the rapid monotonic decrease in pressure and kinetic temperature in expanding flows causes large departures from equilibrium in the vibrational degree of freedom (DOF). In expanding flows, low translational and high vibrational temperatures produce processes of collisional de-excitation which differ from those under normal shock conditions. Experiments show[1-4] that the relaxation time for diatomic molecules in an expanding flow can be 1 to 2 orders of magnitude shorter than the relaxation time behind a shock front.

In flows behind a normal shock, the upper vibrational levels are initially underpopulated due to low vibrational temperature, and the relaxation rate is controlled primarily by the $v = 0 \rightarrow 1$ excitation rate. This process occurs with low probability because of the large energy quanta involved. As the vibrational temperature increases, the transitions from the higher vibrational states start to affect the relaxation process. At higher equilibrium temperatures, a larger role is played by the high vibrational levels in the final stages of the relaxation. In fact, the success of the average temperature formulation $T_a = \sqrt{TT_v}$, in the rate equations as suggested by Park,[5] lies in the fact that it allows the reaction rates to be small at the initial stages of relaxation and to grow exponentially near the final stages of the process.

In expanding flows the molecules relax from a state of high initial population in the upper states. The closer spacings of these levels due to the anharmonicity enables the corresponding smaller quanta to be transferred to the translational mode upon collision. At the same time, due to lower translational temperature, the excitation process to these vibrational levels is inefficient in expanding flows. Consequently, net rapid depopulation of high vibrational levels could explain the faster drain of the vibrational energy in an expansion. In the most simplistic model to account for this rapid relaxation, one uses the linear Landau-Teller vibrational relaxation equation[3,4]

$$\frac{\partial \varepsilon(T_v)}{\partial t} = \frac{\varepsilon(T) - \varepsilon(T_v)}{\tau_v}, \qquad \tau_v = \frac{\tau_s}{\phi} \tag{1}$$

where τ_s is the Landau-Teller relaxation time constant derived from experiments behind normal shocks, ε is the energy per unit mass, and ϕ is a constant.

Proposed values for ϕ, based on experimental data,[3] range between 1–1000 for CO and between 1–70 for N_2. The role of vibration-vibration (V-V) transitions has been pointed out by many investigators[6-8] as the possible cause of this discrepancy. It was suggested that due to rapid V-V transfers among high vibrational levels, the populations tend to get redistributed to a highly nonBoltzmann distribution, and it is no longer possible to describe the relaxing molecules by a single vibrational temperature. In fact, recent computations based on SSH (Schwartz, Slawsky, and Herzfeld) formulations[9] by Sharma et al. indicate that during relaxation in an expanding flow, the high vibrational states quickly equilibrate among themselves, and in a dissociating gas, with the atomic populations. The "distorted population distribution"[6,7] of high vibrational states and the rapid drop in the translational temperature seem to play equally important roles in the relaxation of the expanding flows. It should be pointed out that this redistribution primarily occurs by V-V collisions and, therefore, does not cause any removal of vibrational quanta. Bray[7] classified this distorted population distribution of the high vibrational levels as a "nonisothermal effect" and suggested that the flow history is a contributing factor.

Even today, experimental data on these phenomena in expanding flows are insufficient, and it is difficult to construct any meaningful physical model of the relaxation process. Therefore, more experimental and theoretical investigation is needed to characterize the relaxation phenomena in expanding flows.

At NASA Ames we have launched an experimental program to investigate some relevant aspects of these phenomena. Measurement of the nonequilibrium populations in in-

Presented as Paper 92-0809 at the AIAA 30th Aerospace Sciences Meeting, Reno, NV, Jan. 6–9, 1992; received Jan. 24, 1992; revision received April 23, 1992; accepted for publication April 27, 1992.

*Research Scientist. Associate Fellow AIAA.
†Research Scientist. Member AIAA.
‡Graduate Student. Student Member AIAA.

dividual vibrational energy levels is the most desirable technical approach to this investigation. Spontaneous Raman scattering, in which the molecules in each of vibrational and rotational energy levels modulate the incident laser frequency, can provide the needed data on the nonequilibrium populations at any given instant. For this purpose NASA Ames's electric arc-driven shock-tube facility has been converted into a shock-tunnel facility by installing a two-dimensional nozzle insert in the driven tube. Before conducting the Raman experiment, the flowfield of the two-dimensional nozzle must be characterized. Towards this end we have 1) photographed the density field in the nozzle with holographic interferometry, and 2) computed the flow with a two-dimensional code with a chemically reacting flow model and a one-dimensional code in which the fluid equations are coupled with the master equations describing individual vibrational levels, but no chemical reactions are included. In this article we present the experimental results based on the interferograms and the results of the computations. This presentation is aimed at providing the following: 1) an experimental measurement of the density flowfield of a two-dimensional nozzle; 2) assessment of the capability of the one-dimensional fluid code coupled with the 57 vibrational master equations for possible use in the data analysis of the planned Raman experiments—due to the high cost of two-dimensional or three-dimensional fluid codes coupled with master equations, only a one-dimensional code can be used for this purpose, therefore, before applying a code for the data analysis of the Raman experiment, we must know its limitations; and 3) an assessment of the capabilities of a two-dimensional fluid code.

II. Experimental Facility

The experiments were conducted at NASA Ames's electric arc-driven shock-tube facility. The operating characteristics of the facility have been described in detail in Ref. 10. For completeness, however, we will mention some of its relevant features. The shock-tube driver is powered by a 0.6-MJ, 40-kV capacitor bank. With the use of various driver gas and driver configurations, the facility is capable of producing shock velocities in the range of 2–50 km/s. The 10-cm aluminum driven section of the facility is converted into a reflected shock-tunnel facility by installing a two-dimensional nozzle insert in the tube (Fig. 1). The nozzle, with a throat height of 0.635 cm, has a quadratic profile downstream of the throat and an elliptical shape upstream of it. The quadratic profile is of the form

$$\text{Height} = \tfrac{1}{4}(x^2 + 1), \qquad 0 \le x$$

where x is the axial distance measured from the throat of the nozzle in inches (Fig. 2). The nozzle is about 5-cm wide. A 3.2-km/s shock in 100-Torr nitrogen reflects off the nozzle insert, producing a reservoir of stagnated test gas in the reflected shock region at about P_0 = 1375–1550 psi and T_0 = 7200 K.

A Nd:YAG laser doubled to 532 nm with a 25-ns laser pulse was used to record holograms of the expanding flow

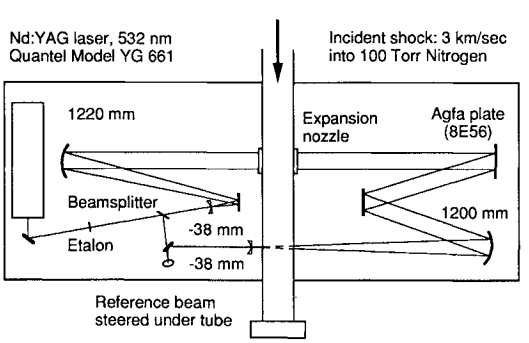

Fig. 1 Holographic interferometry layout.

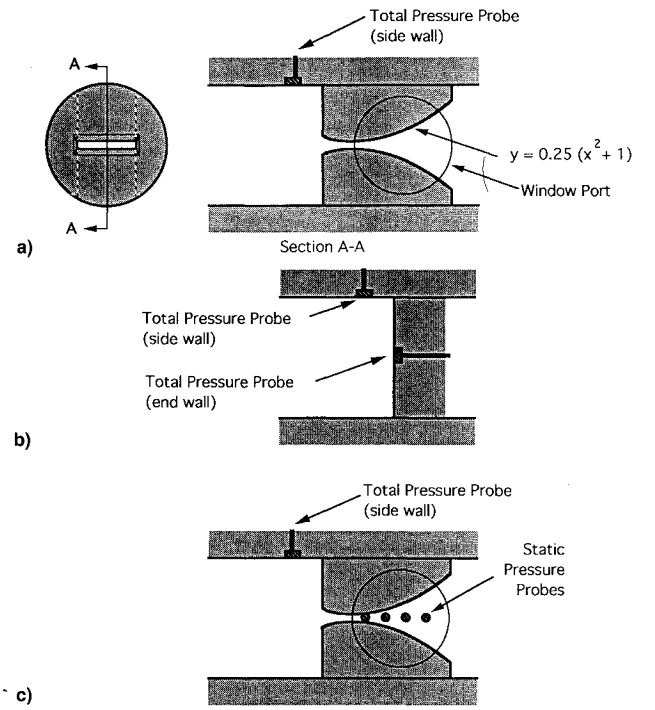

Fig. 2 Two-dimensional nozzle profile: a) holography setup, b) end-wall pressure measurements, and c) static pressure measurements.

from the throat to A/A^* = 10 in the 8-cm nozzle. A schematic of the holographic setup is shown in Fig. 1. The laser beam is split into an object beam and a reference beam. Both beams are expanded and collimated, with the object beam passing through the test section and the reference beam outside the driven tube. Both beams fail onto an Agfa 8e56 film plate. The path lengths of the two beams are matched, and an etalon is placed before the beamsplitter to ensure that the coherence length of the laser is larger than the path difference between the two beams. The film is exposed twice; a reference exposure before the test (no flow) and another exposure during the test. The optical window is big enough to cover the entire nozzle length from the throat to the exit plane (Fig. 2a).

Interferograms are reconstructed from the single-plate, double-exposure holograms on a secondary reconstruction optical setup using an Argon ion laser.

Pressure probes are installed in the reflected shock area to record the reservoir pressure both at the driven tube wall and at the reflective surface of the nozzle insert (Fig. 2b). Pressure probes are also installed in the nozzle wall to record the nozzle static pressure (Fig. 2c). One of the stagnation pressure signals is used as a trigger signal to activate various electronics in the data acquisition system.

III. Numerical Models

A. Two-Dimensional Model

Calculations of the thermochemical nonequilibrium nozzle flowfield were performed with a modified version of the code developed by Palmer.[11] This solver has fully coupled finite-rate chemistry, upwind differencing, and uses an explicit time-marching solution algorithm. In the present study, the species concentrations of N_2 and N are solved using a two-temperature $\sqrt{TT_v}$ model and reaction rates obtained from Park.[5] Binary diffusion is assumed and the vibrational energy transfer rate is determined by the original Landau-Teller model. In order to provide adequate resolution of the boundary layer, especially in cold wall simulations, second-order accurate spatial differencing is required. Thus, the differencing scheme described in Ref. 11 was upgraded to second-order accuracy. Because no shocks are present in the steady-state nozzle flow, no flux limiters were required and second-order accuracy is

maintained throughout the interior of the computational domain.

The inflow plane for the two-dimensional nozzle computations is just downstream of the shock reflection wall of the nozzle insert. At the inflow plane an equilibrium chemical composition is assumed, and vibration is assumed to be in equilibrium with the translational/rotational mode. At this station, total pressure, total temperature, and flow angle are specified and a subsonic characteristic boundary condition is enforced. The nozzle calculations were performed on a 32 × 23 grid modeling one-half of the symmetric nozzle geometry, and the initial flow condition specified was uniform flow.

B. Quasi-One-Dimensional Model

In order to study the details of the vibrational relaxation process, one must solve vibrational master equations. Calculations of this sort will be compared with Raman scattering data (once available) to study various transition rate and relaxation models. However, calculation of all the transition probabilities and rates even for one temperature is computationally expensive. In a general two-dimensional or three-dimensional flow we would need to compute these for every temperature in the flowfield, solve a vibrational rate equation for each vibrational level, and solve fluid dynamic equations simultaneously. Nitrogen has 57 bound quantum states so we would need to solve over 60 coupled equations for each grid node. Thus, detailed calculations of the vibrational transition rate equations in general two-dimensional or three-dimensional flows are prohibitively expensive.

In the present calculations we make the quasi-one-dimensional approximation. This approximation greatly reduces the CPU requirement relative to two-dimensional and three-dimensional calculations because the number of gird nodes and equations are reduced. At present, calculations of the nozzle flow using a quasi-one-dimensional solver are performed to determine if the bulk properties can be predicted while enforcing the quasi-one-dimensional approximations. The flow is assumed to be in steady state and inviscid. At present, the code also assumes that the flow is composed of a pure diatomic gas with no chemical reactions.

C. Vibrational Rate Equations

The vibrational transition rate master equations are of the form

$$\frac{D(N_v/\rho)}{Dt} = \left(\frac{N}{\rho}\right) \sum_{v'=0}^{v_{max}} (K_{v',v}N_{v'} - K_{v,v'}N_v) \tag{2}$$

where N_v is the number of molecules in state v per unit volume. $K(v', v)$ is the rate coefficient for the $v' \rightarrow v$ vibrational transition and $K(v, v')$ for the $v \rightarrow v'$ transition given in the units of $cm^3 s^{-1}$. We can then use fluid transport relations to convert the material derivative to finite-volume form and write the quasi-one-dimensional, steady, vibrational transition rate equation as

$$\frac{\partial N_v}{\partial x} = \left(\frac{N}{U}\right) \sum_{v'=0}^{v_{max}} (K_{v',v}N_{v'} - K_{v,v'}N_v) - \frac{N_v}{A}\frac{\partial A}{\partial x} - \frac{N_v}{2U^2}\frac{\partial (U^2)}{\partial x} \tag{3}$$

The streamwise velocity is U and the nozzle cross sectional area is A. The vibrational energy per unit mass is

$$\varepsilon_{vib} = \frac{1}{\rho} \sum_{v=0}^{v_{max}} E_v N_v$$

In the present calculations E_v and thus ε_{vib} are measured relative to their ground state (i.e., $v = 0$) values. By differentiating this equation and substituting in the previous equation, we can show that the quasi-one-dimensional, steady, vibrational energy rate equation is

$$\frac{\partial \varepsilon_v}{\partial x} = \left(\frac{1}{U}\right)\frac{R}{x} \sum_{v=0}^{v_{max}} \sum_{v'=0}^{v_{max}} (K_{v',v}N_{v'} - K_{v,v'}N_v) \tag{4}$$

where k is Boltzmann's constant and R is the ordinary gas constant.

D. Solution Algorithm

Although we have made the quasi-one-dimensional approximation, if typical time marching numerical schemes are used to solve the finite-difference form of the governing equations, the calculations would still be computationally very expensive. We can take advantage of the quasi-one-dimensional formulation by performing one spatial march rather than iterating in time. For this study an efficient, implicit, space marching solver called STIFF7 is utilized. STIFF7 numerically computes Jacobians and integrates a coupled set of quasilinear, partial differential equations and is described in more detail by Lomax.[12] The above transition rate and energy relaxation equations are coupled with fluid dynamic equations for quasi-one-dimensional, steady-state flow. The use of STIFF7 in nozzle flow computations and additional details of the present quasi-one-dimensional solver are given by Ruffin and Park.[13]

E. Landau-Teller Model

We can also use the present solver to investigate the performance of the Landau-Teller equation. This is done by omitting the population distribution equations, and instead of using the true energy rate equation we use the Landau-Teller relaxation equation [Eq. (1), with $\phi = 1.0$], in the following form:

$$\frac{\partial \varepsilon(T_v)}{\partial x} = \frac{1}{U}\frac{\varepsilon_{vibE} - \varepsilon_{vib}}{\tau_s} \tag{5}$$

In this study τ_s is obtained from Millikan and White experimental data. The equilibrium vibrational energy per unit mass for a harmonic oscillator is

$$\varepsilon_{vibE} = \frac{R\theta_v}{\varepsilon^{\theta_v/T} - 1} \tag{6}$$

IV. Measurements

The measured reflected shock region pressures are shown in Figs. 3 and 4. The endwall stagnation pressure signal trace, shown in Fig. 3, was recorded with the nozzle inlet blanked off. The sidewall stagnation pressure signal trace, shown in

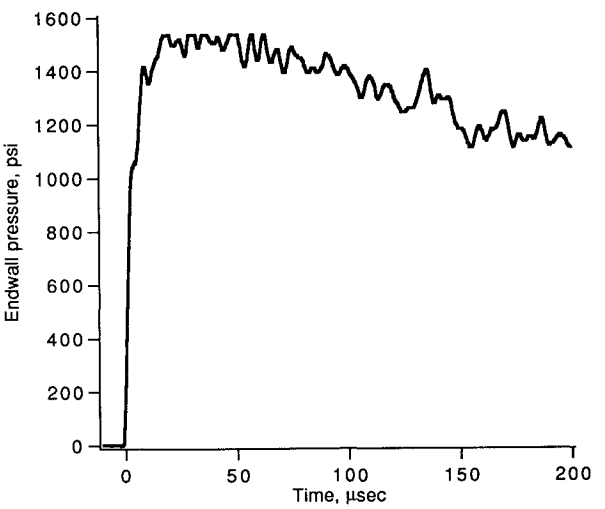

Fig. 3 Endwall pressure at nozzle inlet at a shock velocity of 3.2 km/s in 100-Torr nitrogen.

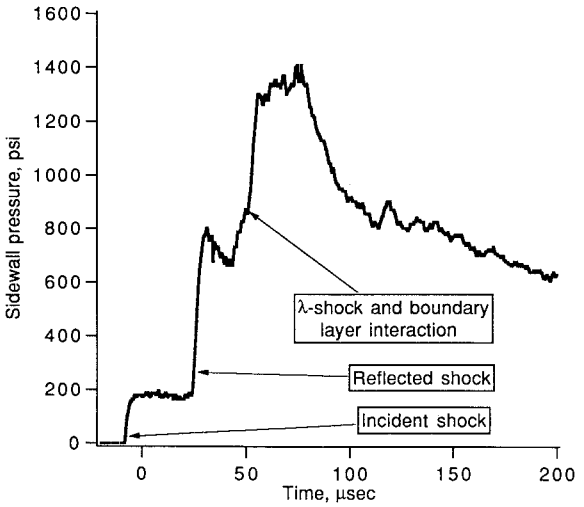

Fig. 4 Sidewall pressure measured about 2.54-cm upstream of the nozzle inlet at a shock velocity of 3.2 km/s in 100-Torr nitrogen.

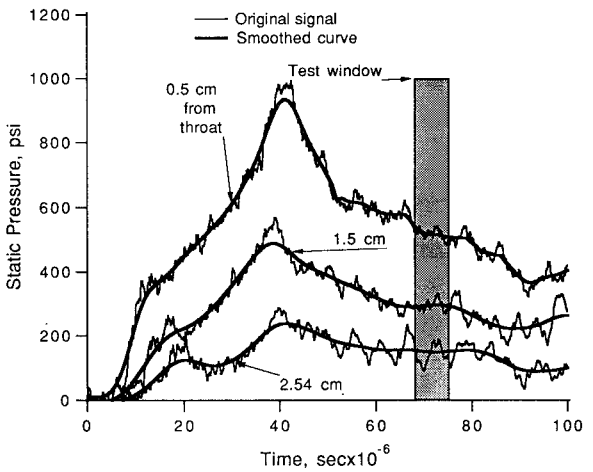

Fig. 5 Static pressures as measured along the axis of the two-dimensional nozzle.

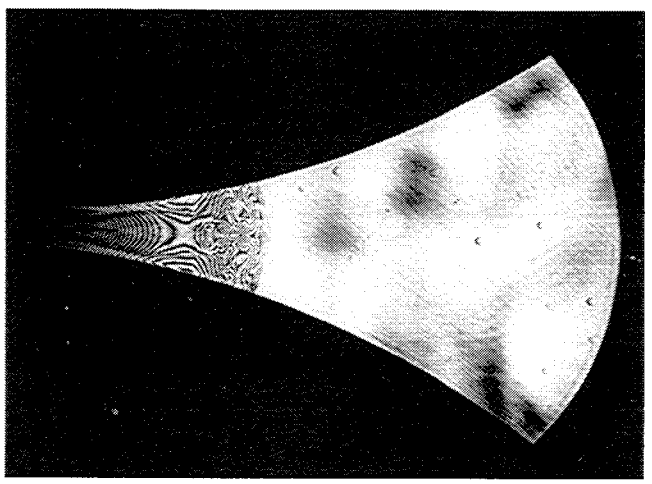

Fig. 6 Interferogram taken at t = 16 μs after the arrival of the reflected shock at station E, P_0 = 1530 psi, T = 7200 K.

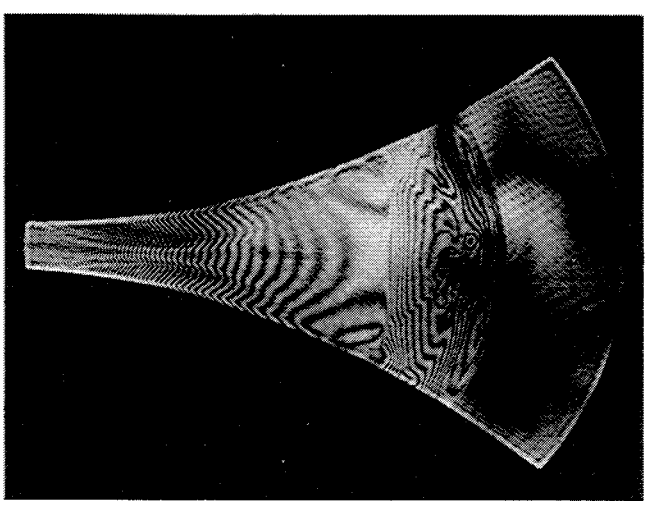

Fig. 7 Interferogram taken at t = 26 μs after the arrival of the reflected shock at station E, P_0 = 1530 psi, T = 7200 K.

Fig. 4, was recorded about 2.5-cm upstream of the endwall (i.e., the nozzle inlet). The sidewall pressure was recorded twice: 1) once with the nozzle end blanked off, and 2) then with the nozzle installed. These two sidewall pressures were close enough to indicate that the recorded endwall pressure (Fig. 3) is a good measure of the stagnation pressure at the inlet of nozzle. As can be seen from Fig. 3, the stagnation pressure at the inlet of the nozzle remains constant to a value of 1530 psi (1.054×10^7 Pa) for about 80 μs. The nozzle residence time in comparison is about 22 μs. The sidewall pressure, which was recorded at a distance of 2.5-cm away from the nozzle inlet wall, shows the complete history of shock arrival and reflection (Fig. 4). The first steep rise in the pressure is due to the arrival of the incident shock, and the second steep rise was due to the reflected shock. However, due to the interaction of the boundary layer and the reflected shock near the wall, the pressure takes some time to reach the reflected shock values, as shown by the peak pressure shown in Fig. 4. The λ-shock and boundary-layer interactions of this type were first observed by Mark[14] and later explained by Sanderson.[15] The cause of the interaction is that the boundary layer behind the incident shock wave has, over a certain range of Mach numbers, insufficiently high total pressure to enable it to pass under the reflected shock. Mark[14] postulated that the boundary-layer fluid collects under the reflected shock which would then bifurcate to form a λ-shock. The front leg of the reflected λ-shock is weaker and the hind leg is stronger than the reflected shock in the core of the shock front. As a result, the pressure signal recorded in the boundary layer shows 1) at first a steep rise due to the weaker shock; 2) then a steep rise due to the stronger shock (overshoot); and 3) then the final value corresponding to the reflected shock in the core of the shock front.

The sidewall pressure signal was used as a trigger source to activate various electronics including the laser pulse at desired times. The time zero in experiment is taken as the time when the incident shock arrives at the nozzle inlet (Fig. 4).

The measured static pressures recorded at x = 0.48, 1.52, and 2.54 cm (x = 0 at the throat) along the nozzle axis are shown in Fig. 5. As can be seen from the figure, the pressures overshoot during the startup process and then reach a steady state at about t = 65 μs, lasting for about 12 μs.

Interferograms were taken at t = 16, 26, and 66 μs and are shown in Figs. 6–8, respectively. In Figs. 6 and 7 the startup processes of the nozzle, such as a normal shock and various oblique shock patterns and expansion waves in the throat area, can be seen. At t = 66 μs (Fig. 8) the flow in the nozzle achieves a steady state and prominent features of a nozzle flow are visible in this interferogram. As the density decreases towards the exit of the nozzle, the fringe spacing in the interferogram increases. The curvature of fringes in the core flow, especially towards the nozzle exit, indicate the two-dimensional nature of the flow and are due to the negative density gradient towards the wall. The boundary-layer effects near the wall are also visible in the interferogram. Due to the cold wall the density gradient changes sign and subsequently the reversal of the fringe pattern.

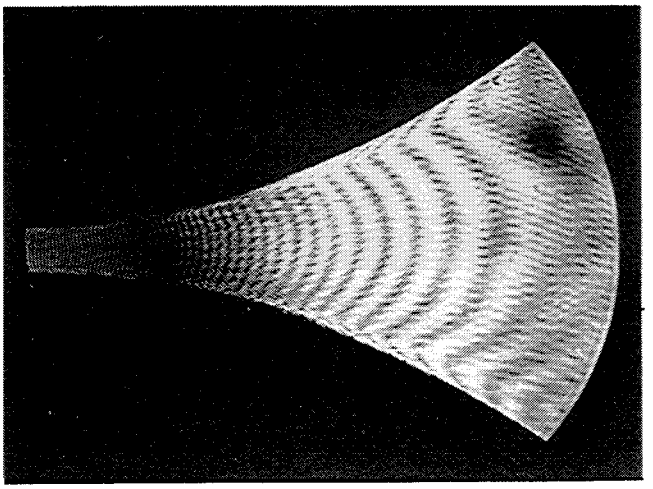

Fig. 8 Interferogram taken at $t = 66$ μs after the arrival of the reflected shock at station E, $P_0 = 1530$ psi, $T = 7200$ K.

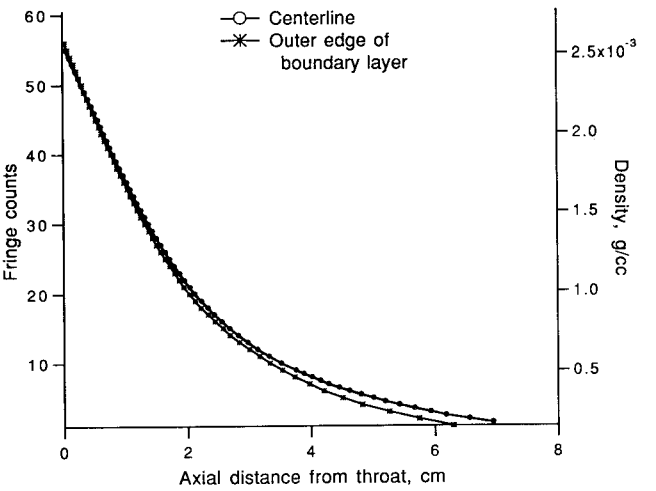

Fig. 9 Fringe counts and density along the centerline and at the outer edge of the boundary layer near the wall as functions of axial distance.

V. Analysis

A. Synthetic Interferograms

The fringe pattern of the interferogram taken at $t = 66$ μs was analyzed. Since the fringe spacings are proportional to the density gradients—knowing a reference density—it is possible to deduce the density at a given point by analyzing the fringe patterns. From the interferograms we obtain 1) fringe count as a function of axial distance for the points along the nozzle axis; 2) fringe count as a function of axial distance for the points at the outer edge of the boundary layer; and 3) fringe pattern in the boundary layer. The first two items are plotted in Fig. 9. The fringe pattern in the boundary layer may provide two basic types of information: 1) the thickness of the thermal boundary layer, and 2) the density gradient in the boundary layer.

In order to utilize the obtained experimental data in assessing our computation capabilities, at first we used the two-dimensional fluid code to compute the nozzle flow for two stagnation conditions: case a, $P_0 = 1530$ psi (1.054×10^7 Pa), $T_0 = 7200$ K; and case b, $P_0 = 1530 \times 0.90 = 1377$ psi (0.949×10^7 Pa), $T_0 = 7200$ K. $T_0 = 7200$ K is used in both cases and is a value obtained from shock-tube relations for a shock velocity of 3.2 km/s in 100-Torr nitrogen using a Lighthill gas model. Case a parameters correspond to the experimentally measured quantities, whereas the selection of case b pressure was arbitrary and was taken to be 90% of the experimentally measured pressure. The importance of case b parameters will be clear when we discuss the static pressure measurement in the nozzle.

The computations were performed for two types of wall conditions: 1) adiabatic wall, and 2) isothermal wall. For isothermal wall, the gas temperatures at the wall T_w were varied from 300–5000 K. (The wall is colder than the gas with heat being transferred to the wall.) Using the computed density flowfield, synthetic interferograms[16] were generated. The synthetic interferograms were then compared with the experimental interferogram. For both cases a and b, wall conditions were varied until the fringe structure in the boundary layer (by visual inspection) agreed with those in the experimental interferogram. In both the cases this was achieved by using the isothermal wall condition with $T_w = 3000$ K. The resulting synthetic interferogram for case a is compared to the experimental one in Fig. 10. The upper half is taken from the experimental interferogram and the lower half is the synthetic one. As we can see from the composite, the fringe structure of the synthetic interferogram agrees well with the experimental one, including the boundary-layer structure. A similar composite is shown in Fig. 11 for case b. Agreement between the two interferograms is not as good.

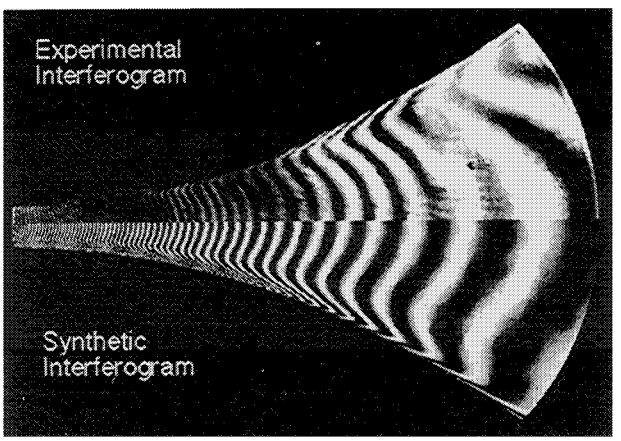

Fig. 10 Synthetic interferogram generated from the data computed using the two-dimensional code. $P_0 = 1530$ psi, $T_0 = 7200$ K.

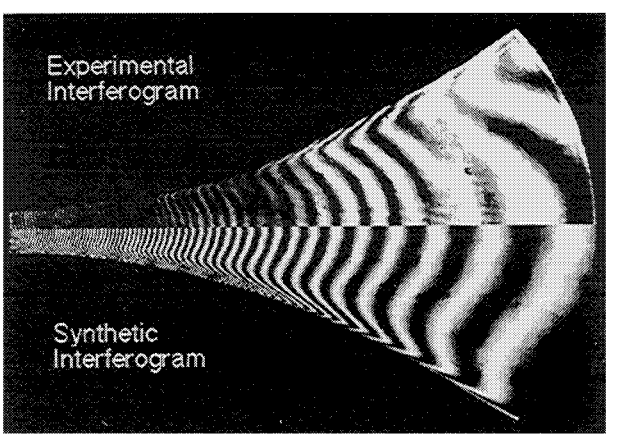

Fig. 11 Synthetic interferogram generated from the data computed using the two-dimensional code with $P_0 = 1377$ psi, $T_0 = 7200$ K.

The fringe counts from the two synthetic interferograms are plotted in Figs. 12 and 13. The fringe counts in Fig. 12 are conducted along the centerline, and along the outer edge of thermal boundary layer in Fig. 13. The plots confirm that the synthetic interferogram for case a is in agreement with the experimental data.

Therefore, based on the interferograms, we suggest that the two-dimensional code is able to compute the flowfield reasonably well using the inputs derived from the experimental data, i.e., $P_0 = 1530$ psi (1.054×10^7 Pa), $T_0 = 7200$ K.

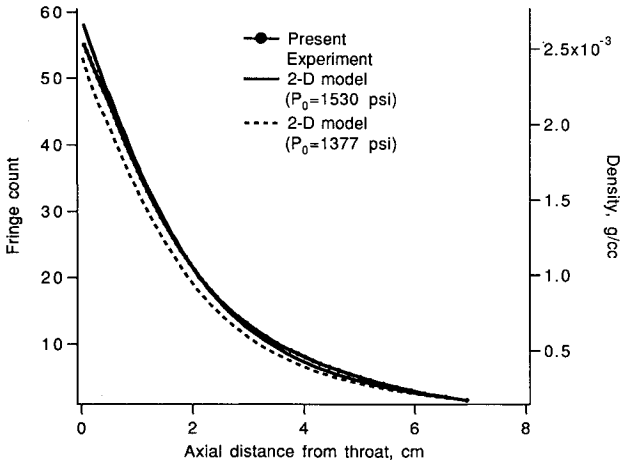

Fig. 12 Fringe counts and density for the centerline derived from the synthetic and experimental interferograms.

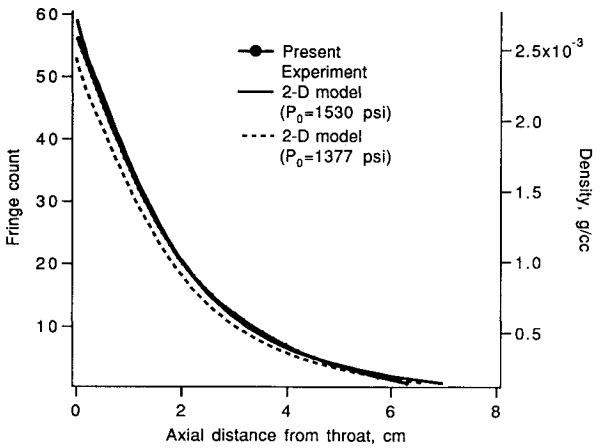

Fig. 13 Fringe counts and density for the points at the outer edge of the boundary layer derived from the synthetic and experimental interferograms.

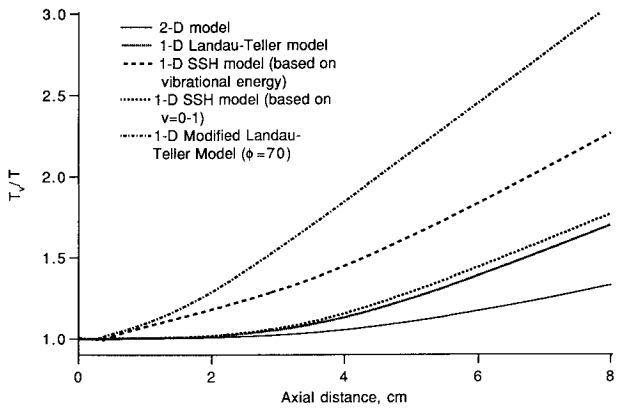

Fig. 14 Vibrational temperature along the nozzle axis.

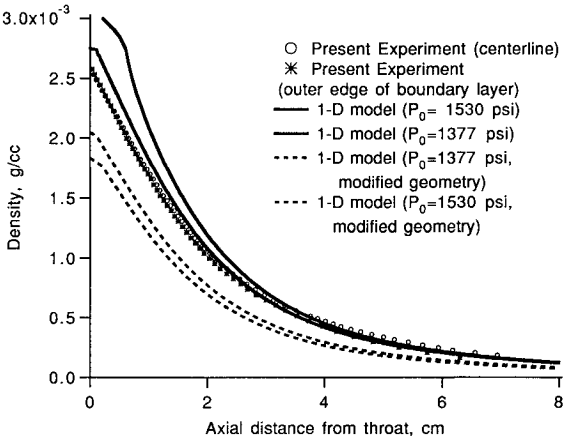

Fig. 15 Results of the one-dimensional model compared with the experimental data.

B. Density Flowfields

The results of the two-dimensional computations were used to determine the reference density (at the nozzle exit) for the experimental interferogram, and the fringe counts were converted into the density of the gas and plotted (see righthand axis, Figs. 9, 12, and 13).

Now we examine the results of the one-dimensional computations. At first we compare the results of the SSH formulations against the Landau-Teller model. The computations were conducted for the case b input conditions [P_0 = 1377 psi (0.949 × 10^7 Pa), T_0 = 7200 K]. As can be seen from the figure, the difference between the results is not noticeable. From here on we will not differentiate between the SSH model and the Landau-Teller model, and both will be called the one-dimensional model.

The degree of the vibrational nonequilibrium, predicted by the two-dimensional and one-dimensional models, can be compared by the plots shown in Fig. 14. In this figure, the vibrational temperature normalized by the local translational temperature (T_v/T) is plotted for the points on the nozzle axis. The vibrational temperature is defined in two ways: 1) based on two lower (v = 0, 1) vibrational levels, and 2) based on the average vibrational energy [Eq. (6)]. The computed nondimensional vibrational temperature T_v/T, irrespective of the model used, increases as we move from the throat to the nozzle exit. However, this increase is modest if the Landau-Teller relaxation model is used.

The SSH model predictions also show a modest increase in this parameter if the vibrational temperature is computed based on the ground state populations (v = 0, 1). But by examining the curve where T_v is computed, based on the average vibrational energy, we find that the SSH model predicts a considerably faster increase in the relative energy stored in the vibrational modes as we move towards the nozzle exit. The modified Landau-Teller [ϕ = 70, Eq. (1)] predicts even faster growth in this energy. It should be pointed out that ϕ = 70 used in the modified Landau-Teller model is based on the experimental data,[7] but the vibrational temperature measurements were based on relatively lower levels. The SSH model, on the other hand, solves for all the vibrational levels to account for their relative contributions and scales up (or down) all the transition rates so that the transition rates for the ground levels match with Millikan and White's experimental data.[17]

The computed densities using the one-dimensional model, for cases a and b inputs, are compared with the experimental data in Fig. 15. In order to compensate for the boundary-layer effects, one-dimensional cases were rerun with a modified geometry correcting it for the boundary-layer displacement thickness. The displacement thickness was computed using the corresponding two-dimensional data. The results of these reruns are labeled as "modified geometry" in the plot. As we can see, none of these predictions agree very well with the experimental data. However, we must point out two important observations: 1) the results from the one-dimensional code are very sensitive to the area modifications, and 2) experimentally measured density falls halfway between the one-dimensional result based on the original geometry and the result based on the modified geometry.

The computed densities using the modified Landau-Teller model in the one-dimensional code for cases a and b are compared with the experimental data in Fig. 16. None of these predictions agree well with the experimental data either.

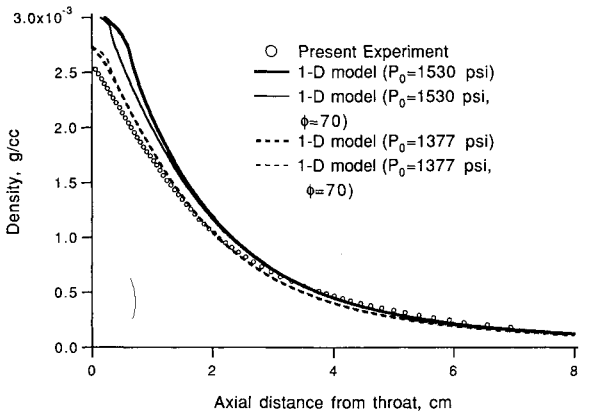

Fig. 16 One-dimensional computations based on modified Landau-Teller model compared with the experimental data.

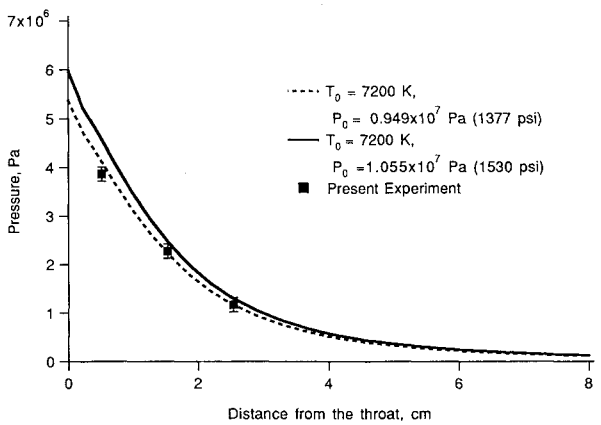

Fig. 17 Measured static pressures compared with the two-dimensional code predictions.

C. Pressure Flowfields

The measured static pressures in the nozzle channel are compared with the two-dimensional predictions in Fig. 17. The experimental data agree better with the case b computed pressures (P_0 = 1377 psi, T_0 = 7200 K). Strong two-dimensional effects were seen in pressure contours generated by the two-dimensional code, which could partially explain the discrepancy between the one-dimensional and the two-dimensional, as discussed in the previous section.

VI. Discussion

There may be another phenomenon which could be responsible for the discrepancy between the computed results and experimental measurements. As seen in Figs. 3 and 5, the steady-state flow is very short-lived. It may be possible that the startup time of the flow is, in reality, slightly larger than is apparent from the holograms and 80 μs of test time ($P_0 \sim$ const) is not enough to truly establish a steady-state nozzle flow. The fact that near the throat region experimental density is slightly lower than case a computations, and the experimental pressure data agrees better with the case b computations, supports this possibility of a drop in reservoir pressure during the test. In order to investigate this possibility and also to have more predictable test times, use of the cylindrical driver[10] for future tests is currently being considered.

A closer examination of interferograms shown in Figs. 10 and 11 reveal that the computed boundary-layer thickness, based on the density gradient structure, is different from the measured one. The experimentally measured thickness near the throat is about 0.53 mm compared to 0.88 mm from the computations; and near the exit it is about 4.37 mm compared to 2.1–2.4 mm from the computations. The discrepancy between the computed density and the experimental data near the throat region may be due to these errors in the boundary-layer (thermal) computations. The errors in the boundary-layer computations may be due to improper inflow conditions, which are determined by trial and error. The throat area is very small and is affected by errors in boundary-layer computations more severely than the exit area.

As mentioned above, due to the lack of a more accurate heat transfer model, we have used an isothermal wall model. In reality, the throat area gets hotter than the exit area, and the assumption of a uniform gas temperature along the wall is not valid. In view of that we ran a case with the two-dimensional code for which the temperatures at points between the throat and the nozzle exit were assumed to be linearly distributed between 3000–300 K. Even this model could not simulate the fringe structure seen in the exit area of the experimental interferogram. In other words, for this given case, the trial and error method may not provide us with the correct simulation. From the present analysis it appears that in order to accurately simulate the flowfield a correct heat transfer model must be applied to the two-dimensional code.

Now it appears that in order to compute the flow correctly the one-dimensional code has to address two major physical phenomena: 1) the two-dimensional effects, and 2) the heat transfer in the boundary layer. As was demonstrated by the one-dimensional computations with the modified nozzle geometry, the effects of the two-dimensional behavior of the nozzle flow on the computed one-dimensional density can be compensated by some minor modification to the nozzle geometry. These modifications could be guided by the two-dimensional computations. After the heat transfer problems of the two-dimensional code are solved the two-dimensional code may be used to modify the flow input conditions, which when used in the one-dimensional code along with the geometry modifications, will result in correct computations of the bulk parameters. In other words, the codes will have to be run interactively.

VII. Conclusions

The density field for a two-dimensional nozzle has been measured. The data are for a A/A^* = 10 nozzle with a quadratic profile. The two-dimensional model used to simulate the nozzle flow is able to compute the flowfield near the exit with reasonable accuracy. An isothermal gas temperature at the wall of T_w = 3000 K is assumed. In order to simulate the throat area correctly, the heat transfer model needs improvement. Also, the validity of the steady-state conditions in the nozzle needs to be verified. The one-dimensional model requires geometrical and input condition modifications in order to simulate the nozzle flow correctly.

References

[1]Blom, A. P., Bray, K. N. C., and Pratt, N. H., "Rapid Vibrational De-Excitation Influenced by Gasdynamic Coupling," *Astronautica Acta*, Vol. 15, Pergamon, Oxford, England, UK, 1970, pp. 487–493.

[2]Blom, A. P., "Shock Tube Measurements of Vibrational Energy Excitation and De-Excitation Rates of Carbon Monoxide, Using Infrared Techniques," Ph.D. Dissertation, Univ. of Southampton, Southampton, 1970.

[3]McLaren, T. I., and Appleton, J. P., "Vibrational Relaxation Measurements of Carbon Monoxide in a Shock-Tube Expansion Wave," *Journal of Chemical Physics*, Vol. 53, No. 7, 1970.

[4]Hurle, I. R., Russo, A. L., and Hall, J. G., "Spectroscopic Studies of Vibrational Nonequilibrium in Supersonic Nozzle Flows," *Journal of Chemical Physics*, Vol. 40, No. 8, 1964, pp. 2076–2089.

[5]Park, C., "A Review of Reaction Rates in High Temperature Air," AIAA Paper 89-1740, Buffalo, NY, June 1989.

[6]Treanor, C. E., Rich, J. W., and Rehm, R. G., "Vibrational Relaxation of Anharmonic Oscillators with Exchange-Dominated Collisions," *Journal of Chemical Physics*, Vol. 48, No. 4, 1968, pp. 1798–1807.

[7]Bray, K. N. C., "Vibrational Relaxation of Anharmonic Oscillator Molecules: II. Non-Isothermal Conditions," *Journal of Physics: Atomic and Molecular Physics*, Vol. 3, No. 11, 1970, pp. 1515–1538.

[8]Blom, A. P., Bray, K. N. C., and Pratt, N. H., "Rapid Vibrational De-Excitation Influenced by Gasdynamic Coupling," *Astronautica Acta*, Vol. 15, No. 5, pp. 487–493.

[9]Sharma, S. P., Huo, W. M., and Park, C., "The Rate Parameters for Coupled Vibration-Dissociation in a Generalized SSH Approximation," AIAA Paper 88-2714, Buffalo, NY, June 1988.

[10]Sharma, S. P., and Park, C., "Operating Characteristics of a 60 cm and a 10 cm Electric Arc Driven Shock Tube—Part I: The Driver," *Journal of Thermophysics and Heat Transfer*, Vol. 4, No. 3, 1990, pp. 259–265; see also AIAA Paper 88-0142, Jan. 1988.

[11]Palmer, G., "Enhanced Thermochemical Nonequilibrium Computations of Flow Around the Aeroassist Flight Experiment Vehicle," AIAA Paper 90-1702, Seattle, WA, June 1990.

[12]Lomax, H., "Stable Implicit and Explicit Numerical Methods for Integrating Quasi-Linear Differential Equations with Parasitic-Stiff and Parasitic-Saddle Eigenvalues," NASA TN D-4703, May 1968.

[13]Ruffin, S. M., and Park, C., "Vibrational Relaxation of Anharmonic Oscillators in Expanding Flows," AIAA Paper 92-0806, Reno, NV, Jan. 1992.

[14]Mark, H., "The Interaction of a Reflected Shock Wave with the Boundary Layer in a Shock Tube," *Journal of Aeronautical Sciences*, Vol. 24, No. 4, 1957, pp. 304–306.

[15]Sanderson, R. J., "Interprepation of Pressure Measurements Behind the Reflected Shock in a Rectangular Shock Tube," *AIAA Journal*, Vol. 7, July 1969, pp. 1370–1372.

[16]Yates, L. A., "Interferograms, Schlieren, and Shadographs Constructed from Real- and Ideal-Gas, Two- and Three-Dimensional Computed Flow Fields," FY92 Ames Technical Paper Contest for Women, Society of Women Engineers, Orlando, FL, June 1992.

[17]Millikan, R. C., and White, D. R., "Systematics of Vibrational Relaxation," *Journal of Chemical Physics*, Vol. 39, No. 12, 1963, pp. 3209–3213.